Journal of Power Sources 209 (2012) 163–171

Contents lists available at SciVerse ScienceDirect

Journal of Power Sources

journal homepage: www.elsevier.com/locate/jpowsour

Increased ionic conductivity in microwave hydrothermally synthesized rare-earth doped ceria $Ce_{1-x}RE_xO_{2-(x/2)}$

Jesús Prado-Gonjal [a], Rainer Schmidt [b,*], Jesús Espíndola-Canuto [a,c], P. Ramos-Alvarez [a,d], Emilio Morán [a]

[a] Departamento de Química Inorgánica, Facultad de Ciencias Químicas, Universidad Complutense de Madrid, 28040 Madrid, Spain
[b] Departamento Física Aplicada III, Facultad de Ciencias Físicas, GFMC, Universidad Complutense de Madrid, 28040 Madrid, Spain
[c] Centro de Física Aplicada y Tecnología Avanzada, UNAM, 76001 Querétaro, Mexico
[d] Instituto de Investigaciones en Materiales, UNAM, Cd. Universitaria, México D.F. 04510, Mexico

ARTICLE INFO

Article history:
Received 16 November 2011
Received in revised form 1 February 2012
Accepted 21 February 2012
Available online xxx

Keywords:
Microwave-hydrothermal synthesis
Ceramic nanomaterials
Rare-earth doped ceria
IT-SOFCs
Impedance spectroscopy

ABSTRACT

$Ce_{0.85}RE_{0.15}O_{1.925}$ (RE = Gd, Sm), $Ce_{0.8}(Gd_{0.1}Sm_{0.1})O_{1.9}$ and $CeO_{2-\delta}$ nano-powders were synthesized by microwave-assisted hydrothermal synthesis in a time and energy efficient way. The fluorite-type crystal structure of the synthesized nano-powders was confirmed by X-ray diffraction (XRD) and Rietveld refinement, and the nano-metric particle sizes calculated from the XRD line width broadening were consistent with transmission electron microscopy observations. The Brunauer–Emmett–Teller method was used to confirm large powder surface area. Scanning electron microscopy confirmed high density and low surface porosity of the sintered ceramics as a result of the high sintering activity of the large surface area nano-powders. Impedance spectroscopy was carried out to separately analyze grain boundary (GB) and bulk dielectric relaxations where GB areas were found to constitute ionic charge transport barriers, because their resistance was larger than that of the bulk. Such barriers were found to be comparatively low due to high GB and bulk ceramic ionic conductivities, with the highest values encountered in the composition $Ce_{0.85}Sm_{0.15}O_{1.925}$. The optimal ionic conductivities encountered were associated with the effect of high sintering activity of the nano-powders.

1. Introduction

Solid oxide fuel cells (SOFCs) are typically composed of a dense oxygen ion conducting ceramic electrolyte, a cathode and anode made from porous ceramic materials and electrical contacts [1,2]. SOFCs promote pollution-free and more efficient transformation of fuel into electrical power than traditional combustion engines [3]. A major impetus for the development of new electrolyte materials is the desired reduction of the operating temperature of conventional SOFCs of ≈1000 °C to ≈500–800 °C for intermediate temperature solid oxide fuel cells (IT-SOFCs) [4,5]. Ceria-based solid solutions have been regarded promising candidates to serve as electrolytes in IT-SOFCs since their oxygen ion conductivities are higher than that of yttria stabilized zirconia (YSZ) in the intermediate temperature range [6,7]. Gadolinium and samarium-doped ceria have been extensively studied due to their high ionic oxygen conductivity [8,9]. This increased ionic conductivity is a result of chemically doping the parent compound $Ce^{4+}O_2$ with the tri-valent rare-earth (RE) cations Gd^{3+} and Sm^{3+}. The charge compensation mechanism for such alio-valent doping is by formation of oxygen vacancies ($Ce^{4+}_{1-x}RE^{3+}_xSm^{3+}_{0.1}O_{2-x/2}$), which facilitates ionic oxygen vacancy conduction.

One major problem for the application of polycrystalline oxygen ionic conductors as SOFC electrolyte is the ceramic grain boundary (GB) resistance, which is usually larger than or in the same range as the bulk resistance although GB areas are expected to be thin. This implies that GBs constitute barriers for ionic charge transport and they indeed often act as Schottky barriers [10]. Therefore, the reduction of the GB resistance is of uppermost importance to facilitate application of polycrystalline electrolytes. To achieve this, several attempts have been made recently to increase the sintering activity of as-prepared ceria powders by decreasing the particle size to the nanometer range, and the ionic conductivities have been reported to be indeed significantly enhanced in ceramics made from such powders [11,12]. For the synthesis of cation-doped and undoped ceria nano-sized particles several techniques have been developed including urea-based homogeneous precipitation [13], co-precipitation [14], flux method [15], mechanical mixing [16] and hydrothermal synthesis [17].

For hydrothermal synthesis the use of microwave (MW) ovens offers benefits in form of cost savings through the reduction in processing time and energy [18,19], which has successfully been demonstrated for many materials ranging from binary metallic oxides, oxyhydroxides and ternary oxides, to more complex

* Corresponding author. Tel.: +34 91 394 4445; fax: +34 913945196.
E-mail address: rainerxschmidt@googlemail.com (R. Schmidt).

0378-7753/$ – see front matter © 2012 Elsevier B.V. All rights reserved.
doi:10.1016/j.jpowsour.2012.02.082

materials and structures such as zeolites or other mesoporous materials [20–22]. Nanosized ceria powders have been prepared before under microwave-hydrothermal conditions [23] in a two step process of (A) MW irradiation of the precursor solution forming $Ce(OH)CO_3$, and (B) crystallization of the fluorite structure by heat treatment. An improvement of such synthesis technique using a one-step microwave-hydrothermal synthesis process has been demonstrated on rare-earth Pr doped ceria [24], but has not been applied to Sm and Gd doped ceria so far. Sm and Gd doped ceria are preferential though, because their ionic conductivities are superior to any other rare-earth ceria dopant [25]. In a recent publication it had been demonstrated though that the optimum ionic conductivity may be encountered in 2% Ca doped $Ce_{0.78}Ca_{0.02}Sm_{0.2}O_{1.88}$ [26].

In the present work a one-step microwave-hydrothermal synthesis process of $Ce_{0.85}RE_{0.15}O_{1.925}$ (RE = Gd, Sm), $Ce_{0.8}(Gd_{0.1}Sm_{0.1})O_{1.9}$ and $CeO_{2-\delta}$ nano-powders is reported including structural and microstructural characterization of the powders and a comprehensive study of the ionic charge transport in sintered ceramics. In order to assess the role of the GB areas for oxygen ion charge transport, the resistances of the GB and bulk areas were deconvoluted and analyzed separately by fitting impedance spectroscopy data to an equivalent circuit model consisting in a series of two parallel resistor-capacitor (RC) elements, one for the bulk and one for the GB dielectric relaxation processes. Such fitting was performed for data collected at various temperatures and the GB and bulk Arrhenius plots were obtained.

2. Experimental procedure

2.1. Synthesis

Hydrothermal synthesis is a wet-chemical technique, where the precursor solution is placed in a closed vessel and high autogenous pressure in the vessel is achieved by heating the solution above the boiling point; in this study 200 °C was used. Nanosized particle powders can be synthesized at such low reaction temperature, where particle growth is minimized. The main process parameters to be controlled are the chemical reaction of the precursor solution, pH of the solution, reaction temperature and pressure. Such parameters determine the particle nucleation mechanism and growth kinetics, ideally leading to the desired morphology of the crystallites [27,28]. Cerium(III) nitrate hexahydrate $Ce(NO_3)_3{\cdot}6H_2O$, ≥99% (Sigma–Aldrich), samarium(III) nitrate hexahydrate $Sm(NO_3)_3{\cdot}6H_2O$, 99.9% (Sigma–Aldrich), gadolinium(III) nitrate hexahydrate $Gd(NO_3)_3{\cdot}6H_2O$, 99.9% (Sigma–Aldrich) and potassium hydroxide KOH flakes, 90% (Sigma–Aldrich) were used as starting chemicals. The aqueous solutions of each composition were prepared by dissolving the nitrate salt to the desired concentrations in distilled water and dilution in 1.2 M of KOH under constant stirring. The solution was ultrasonically dispersed for 2 min and the reactions were carried out in double-walled vessels consisting of an inner Teflon sealed autoclave and an outer shell high strength polymer. The vessels were placed in a Milestone ETHOS 1 microwave system operated at 2.45 GHz. The heating ramp up to 200 °C was set to ≈12 °C min^{-1}, the holding time at 200 °C was 30 min, which was followed by switching off the microwave power to furnace cool to room temperature at ≈5 °C min^{-1}. The reaction vessel was connected to a pressure transducer in order to monitor the autogenous pressure, which was found to amount to ≈16 bars during the 30 min holding time at 200 °C. The crystallized powders obtained were decanted 3 times, rinsed with distilled water to eliminate the remaining impurities and dried at 80 °C. The dry powders were then compacted into pellets in a uni-axial 2 ton die press for 5 min and densification sintering was carried out at 1450 °C for 4 h followed by slow cooling at 1.5 °C min^{-1}. The density of the pellets obtained were found to be higher than ≈80%.

2.2. Structural and microstructural characterization

Powder X-ray diffraction (XRD) patterns were collected on a Philips XPert PRO ALPHA1 Panalytical B.V. diffractometer with Cu Kα1 monochromatic radiation (λ = 1.54056 Å) equipped with a primary curved Ge111 primary beam monochromator and a speed X'Celerator fast detector, operating at 45 kV and 40 mA. XRD pattern were collected in the 2θ range of 10–120° at room temperature with angle step size of 0.017° ($2-\theta$) and 8 s counting time in order to ensure sufficient resolution for structural refinements by the Rietveld method [29] using Fullprof software.

For scanning electron microscopy (SEM), powder and ceramic pellet samples were sputter coated (EMITECH K550) with Au to enable SEM by using a Jeol 6400 microscope equipped with a detector for energy-dispersive analysis of X-rays (EDAX). Samples for transmission electron microscopy (TEM) were prepared by ultrasonic dispersion of the powder in n-butanol. Drops of this dispersion were deposited on a carbon-coated copper grid. A Jeol-2000FX electron microscope operating at 200 kV was used in order to perform TEM and selected area electron diffraction (SAED).

Specific surface area (SSA) measurements were carried out by the Brunauer, Emmett and Teller (BET) method [30]. Nitrogen adsorption–desorption isotherms were recorded using a Micromeritics ASAP 200 surface analyzer. Prior to the measurements the powder samples were placed in a glass cell and heated in vacuum at 110 °C for 180 min in order to achieve the removal of water and other contaminants by degassing, which is essential to facilitate accurate surface area determination. The BET analysis port was cooled by immersion into a liquid nitrogen dewar in order to maintain constant temperature of 77 K during measurement. Such low temperature is required to ensure sufficient interaction between the gas molecules and the surface of the sample for measurable amounts of adsorption to occur. Nitrogen adsorption layers were formed on the particle surfaces, the sample was removed from the nitrogen atmosphere and the release of the adsorbed nitrogen was quantified during heating. The data collected are displayed in the form of BET isotherms, which plot the amount of gas adsorbed as a function of the relative pressure [31,32].

2.3. Ionic conductivity measurements

For ionic conductivity measurements by impedance spectroscopy (IS) the sintered pellets were covered on both sides with Au electrodes using dc sputtering. IS measurements were carried out at 440 K–560 K using a Novocontrol Alpha-A High Performance Frequency Analyzer equipped with a liquid nitrogen cooled sample chamber. A 100 mV amplitude alternating voltage signal was employed and IS data was obtained at each temperature in terms of the real and imaginary parts of the impedance ($Z' - Z''$) at variable frequency (f) of 10 mHz to 3 MHz. The impedance data was converted into the complex dielectric permittivity notation $\varepsilon' - \varepsilon''$ by using the standard conversion [33] and taking into account the sample dimensions. Equivalent circuit fitting of the dielectric data was performed by using Z-View software.

3. Results and discussion

3.1. X-ray diffraction and Rietveld refinement

Phase purity and the fluorite CeO_2 crystal structure of each sample were confirmed from the powder XRD pattern shown in Fig. 1. The nanometric size of the synthesized powders was evident by

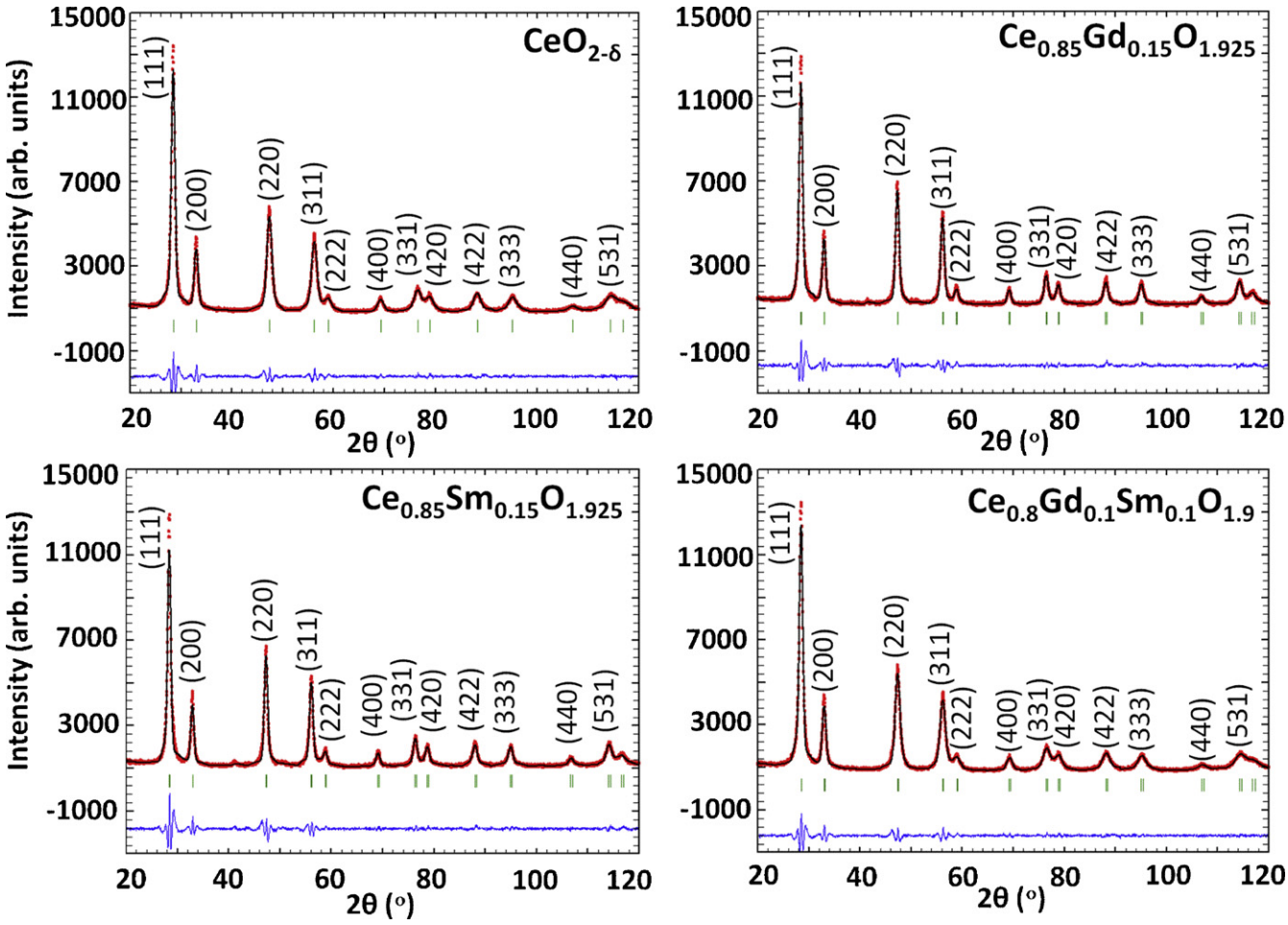

Fig. 1. Rietveld refinement of powder X-ray diffraction patterns: observed (red dotted lines), refined (black solid lines), and their difference (blue bottom line). Green vertical bars indicate the X-ray reflection positions. (For interpretation of the references to color in this figure legend, the reader is referred to the web version of the article.)

perceptible diffraction line broadening. The average crystallite sizes were calculated from the full width half maximum of the (2 2 0) reflection line by using the Debye–Scherrer formula [34]. Approximately 9 nm for $CeO_{2-\delta}$, 10 nm for $Ce_{0.8}Gd_{0.1}Sm_{0.1}O_{1.9}$, 12 nm for $Ce_{0.85}Gd_{0.15}O_{1.925}$ and 14 nm for $Ce_{0.85}Sm_{0.15}O_{1.925}$ were found. Due to equivalent synthesis conditions for all compositions, this moderate increase in crystallite size may be assigned to the role of the rare-earth dopants on the synthesis reaction mechanism. Structural Rietveld refinements yielded satisfactory fits by using the cubic #225 *Fm*−3*m* space group. Fig. 1 shows the collected XRD data, the fitted curves and their differences for all doped and undoped ceria samples investigated. Table 1 shows the results of the performed structural analysis. Numbers in parentheses represent standard deviations. The lattice parameters obtained after data refinement are in good agreement with data reported in the literature [35,36]. All atom positions are fixed by the symmetry of the *Fm*−3*m* space group and were not refined. Rare earth cations are situated at the 4a site with the atomic coordinate (0, 0, 0) and oxygen is at the 8c site corresponding to the (¼, ¼, ¼) position.

Table 1
Unit cell parameters and agreement factors, obtained through Rietveld analysis of the powder X-ray diffraction patterns.

Space group: *Fm*−3*m* (#225)		
	a (Å)	Agreement factors
$CeO_{2-\delta}$	*a* = 5.4211 (1) Å	R_p = 3.65; R_{wp} = 4.87; R_{exp} = 2.75; χ^2 = 3.14
$Ce_{0.85}Gd_{0.15}O_{1.925}$	*a* = 5.4297 (1) Å	R_p = 3.24; R_{wp} = 4.51; R_{exp} = 2.48; χ^2 = 3.31
$Ce_{0.85}Sm_{0.15}O_{1.925}$	*a* = 5.4345 (1) Å	R_p = 3.69; R_{wp} = 5.30; R_{exp} = 2.58; χ^2 = 4.24
$Ce_{0.8}Gd_{0.1}Sm_{0.1}O_{1.9}$	*a* = 5.4259 (2) Å	R_p = 3.28; R_{wp} = 4.31; R_{exp} = 2.72; χ^2 = 2.51

3.2. Microstructural analysis

3.2.1. Transmission electron microscopy (TEM) and scanning electron microscopy (SEM)

TEM images of the synthesized ceria powders show agglomerated particles (Fig. 2) with nanometric size. The corresponding SAED patterns (insets of Fig. 2) show the diffraction rings commonly observed in polycrystalline materials, with the radii inversely proportional to the interplanar spacings d_{hkl} of the lattice planes. The mean particle sizes determined from TEM images are consistent with the XRD particle size calculations described above.

In Fig. 3(a)–(d) SEM micrographs of undoped and doped ceria sintered pellets indicate a dense microstructure. As a result of the densification sintering a massive increase in grain size was observed indicating good sintering activity of the nanopowders. The average grain sizes found were approximately 2.95 μm for $CeO_{2-\delta}$, 3.23 μm for $Ce_{0.85}Gd_{0.15}O_{1.925}$, 2.91 μm for $Ce_{0.85}Sm_{0.15}O_{1.925}$, and 4.06 μm for $Ce_{0.8}Gd_{0.1}Sm_{0.1}O_{1.9}$. It has to

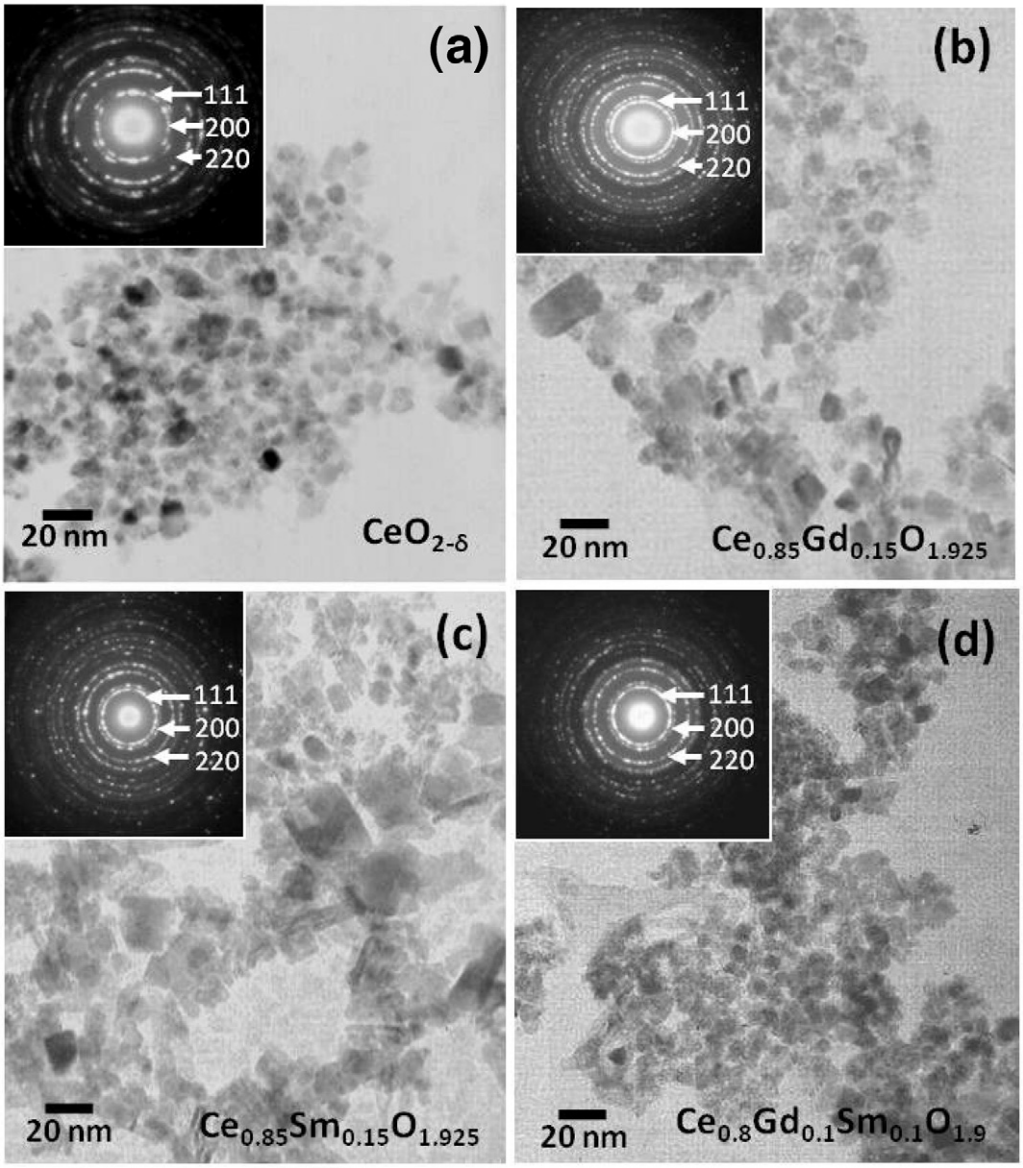

Fig. 2. TEM micrographs and in the top corners the SAED patterns.

be noted though that the grain sizes show the signs of a bimodal or multi-modal distribution to a stronger or lesser extent depending on the cationic dopant (Fig. 3e). Clearly, the different dopant cations play a significant role determining the sintering behavior of the ceramics leading to different grain size distributions, in agreement with previous reports [37].

3.2.2. BET surface area analysis

N_2 adsorption–desorption isotherms of powders are presented in Fig. 4. The plot shows the amount of gas adsorbed ($cm^3\,g^{-1}$) vs. the relative pressure (P/P_o), where P is the equilibrium pressure of the adsorbed vapor and P_o is the saturated vapor pressure at the temperature of the experiment (77 K). These isotherms exhibit a hysteresis loop, where the lower branch represents measurements obtained by progressive addition of gas of the adsorbent, and the upper branch by progressive withdrawal. Such hysteresis is usually associated with the filling and emptying of meso-pores by capillary condensation [38,39]. The lower hysteresis closure point was observed at a relative pressure P/P_o of ≈0.4, which is within the expected range according to the literature [38]. The surface area determination using the BET technique yielded values of $62.2 \pm 0.4\,m^2\,g^{-1}$ for $CeO_{2-\delta}$, $86.6 \pm 0.2\,m^2\,g^{-1}$ for $Ce_{0.85}Sm_{0.15}O_{1.925}$, $89.2 \pm 0.4\,m^2\,g^{-1}$ for $Ce_{0.85}Gd_{0.15}O_{1.925}$ and $97.6 \pm 0.5\,m^2\,g^{-1}$ for $Ce_{0.8}Gd_{0.1}Sm_{0.1}O_{1.9}$. These values imply unambiguously that alio-valent chemical doping increases the ceria surface area. It should be noted though that the powder surface areas from the BET method and the crystallite sizes from XRD and TEM display somewhat different trends. It is suggested that crystallites may agglomerate and in such way the overall BET surface area is not only dependent on the crystallite size but is also strongly influenced by the agglomeration behavior. Agglomeration was indeed indicated in the TEM images presented in Fig. 2 and the surface area trends observed suggest that each rare-earth cation dopant has a distinct influence on the agglomeration behavior and the surface area. The ceria powder surface area trends for different dopants are in agreement though with the average grain sizes of the sintered ceramics determined by SEM (Fig. 3). This may suggests that the surface areas are in fact a quite influential factor in the sintering mechanism. The thermodynamic driving forces determining the sintering mechanism have been reported

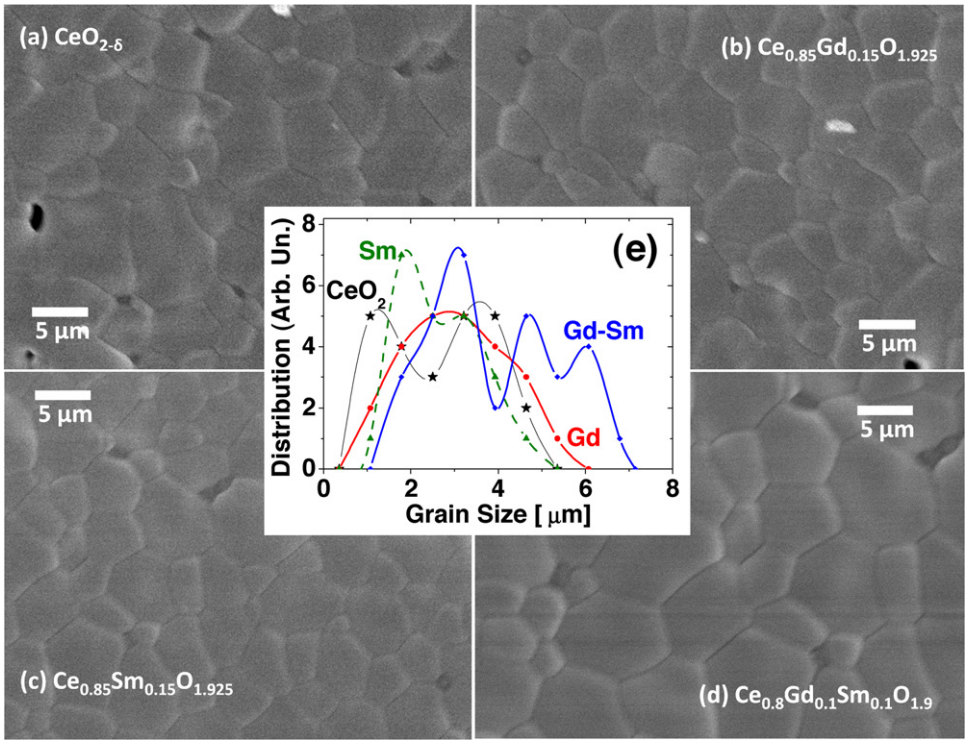

Fig. 3. SEM micrographs of sintered pellets at 1450 °C for 4 h (a–d) and grain size distributions (e).

previously to be associated with changes in the free energy of the surface area of fine powders [40].

Generally, the surface area values obtained were rather high considering the fact that the synthetic route is template free. Previous reports all suggested lower surface area values for materials synthesized by the hydrothermal method (37–80 $m^2\,g^{-1}$) [41], sol–gel (73 $m^2\,g^{-1}$) [42] or a surfactant-free emulsion method (43 $m^2\,g^{-1}$) [43]. In conclusion, the microwave-hydrothermal method appears as an effective route for the synthesis of materials with large surface area and potentially high sintering activity.

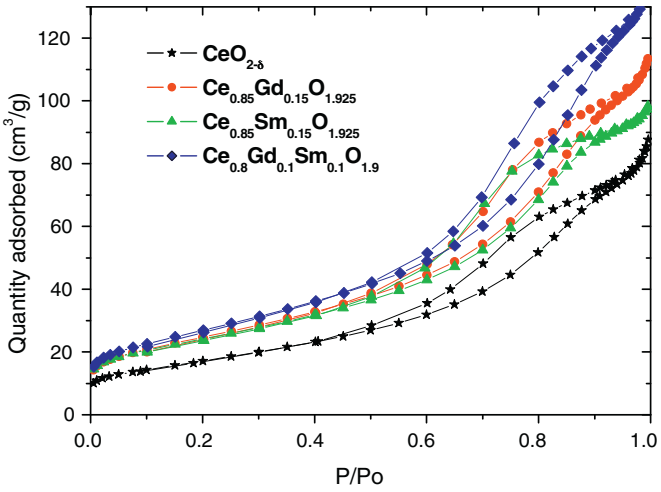

Fig. 4. BET N_2 adsorption–desorption isotherms at 77 K. The amount of gas adsorbed and desorbed ($cm^3\,g^{-1}$) is plotted vs. the relative pressure (P/P).

3.3. Ionic conductivity measurements by impedance spectroscopy

3.3.1. Data presentation and equivalent circuit fitting

Impedance Spectroscopy (IS) data collected for the $Ce_{0.8}Gd_{0.1}Sm_{0.1}O_{1.9}$ sample at 560 K is shown in Fig. 5 in terms of the complex impedance plane plot of $-Z''$ vs. Z'. Two regular semicircles are displayed, which are consistent with a series connection of two conventional dielectric relaxation processes and can, therefore, be modeled by a series of two parallel

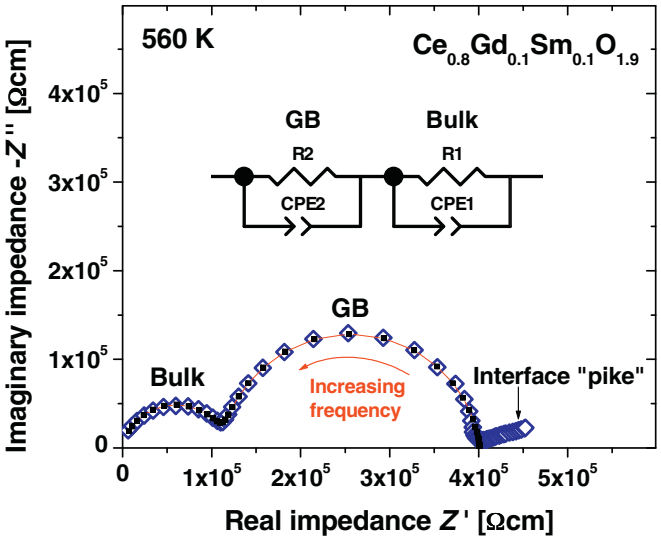

Fig. 5. Complex impedance plot of $-Z''$ vs. Z' for $Ce_{0.8}Gd_{0.1}Sm_{0.1}O_{1.9}$ at 560 K, demonstrating bulk, GB and interface relaxations. Open symbols (◊) represent measured data, squares (■) and solid lines represent equivalent circuit fits at intermediate/high frequency using the model presented in the figure.

resistor-capacitor (RC) elements [44]. The high frequency semi-circle can be ascribed to an intrinsic bulk contribution, whereas the intermediate frequency semi-circle is interpreted as a GB response [42,45]. It should be noted though that the semi-circles in Fig. 5 are slightly suppressed in a way such that the semicircle centre seems to be slightly suppressed below the Z' x-axis. This indicates a certain degree of non-ideality of the relaxation process, which can be accounted for by replacing the ideal capacitor in the RC element with a constant phase element (CPE) [46]. Fig. 5 shows an equivalent circuit consisting of a series of such two non-ideal R-CPE elements and an almost ideal fit was obtained at intermediate and high frequencies. The CPE behavior is usually explained in the framework of a jump-relaxation model [47], or in simpler terms by a broadening of the distribution of relaxation times τ across the macroscopic sample [48], where $\tau = RC$, with R being the resistance and C the capacitance of an ideal RC element.

At the low frequency end the data points in $-Z''$ vs. Z' (Fig. 5) align linearly in a "pike"-like fashion, which is inconsistent with the conventional RC element model and is commonly interpreted as a blocking effect of the electrode sample interface. This constitutes clear evidence for ionic charge transport [49], where the blocking effect of the interface occurs as a result of the different types of dominating charge carriers in the Au electrodes (electrons) and in the ceramics (oxygen vacancies). Therefore, ionic conductivity in the $Ce_{0.8}Gd_{0.1}Sm_{0.1}O_{1.9}$ sample is evident, electronic contributions may be negligible, a potential mixed valence Ce^{3+}/Ce^{4+} electronic hopping conduction is not visible and, consequently, the $Ce_{0.8}{}^{4+}Gd_{0.1}{}^{3+}Sm_{0.1}{}^{3+}O_{1.9}{}^{2-}$ sample may be close to the ideal stoichiometry. The charge transport across blocking electrode interfaces is usually by diffusion, which was not accounted for in the equivalent circuit model here, because rather complex circuit components such as Warburg elements are needed to describe diffusion processes [43].

Fig. 6 displays plots of only the imaginary parts of the impedance $-Z''$ vs. frequency f for the $Ce_{0.8}Gd_{0.1}Sm_{0.1}O_{1.9}$ sample on double-logarithmic axes in order to display the curves for all measured temperatures as indicated. Two dielectric relaxation peaks for the bulk and GB contribution are evident, consistent with the two bulk and GB semi-circles in Fig. 5. The low frequency interface relaxation shows clearly different trends with f, again inconsistent with the standard RC element model and confirming the above interpretation of an electrode blocking effect. The height of the bulk

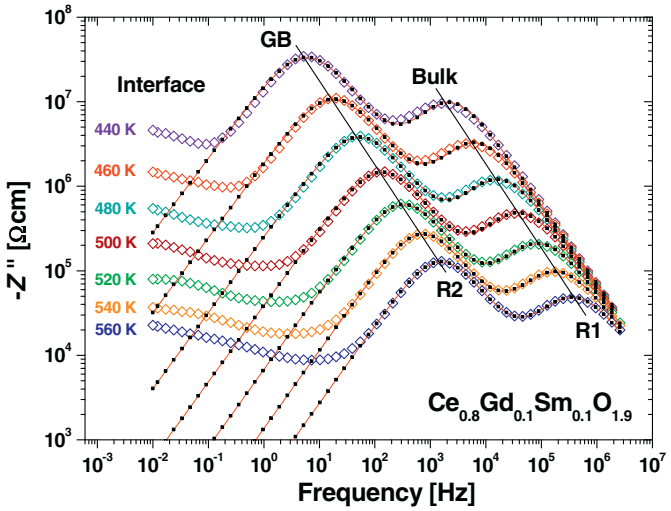

Fig. 6. Imaginary part of the impedance ($-Z''$) plotted vs. frequency for $Ce_{0.8}Gd_{0.1}Sm_{0.1}O_{1.9}$. Two relaxation peaks for the GB and bulk dielectric relaxations are displayed. Both peaks exhibit thermal activation as indicated by solid lines. Open symbols (◊) represent measured data, squares (■) and solid lines represent equivalent circuit fits using the model presented in Fig. 5.

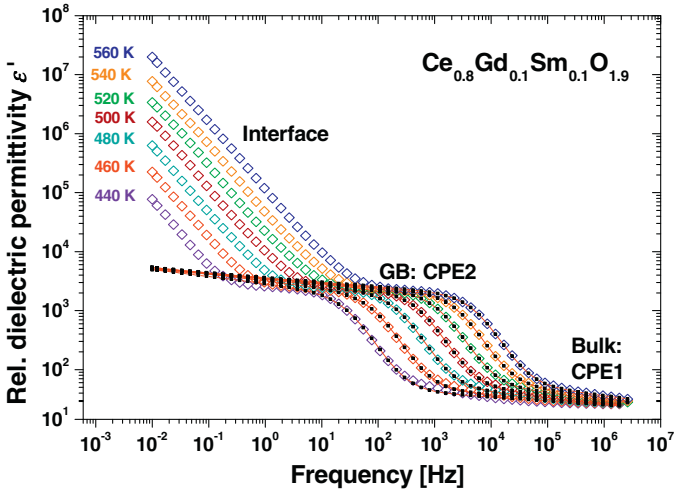

Fig. 7. Relative dielectric permittivity ε' vs. f for $Ce_{0.8}Gd_{0.1}Sm_{0.1}O_{1.9}$. Open symbols (◊) represent measured data, squares (■) and solid lines represent equivalent circuit fits to the data using the model presented in Fig. 5.

and GB relaxation peaks are proportional to the resistance of the respective contribution and the thermal activation of GB and bulk ionic charge transport is indicated by solid lines in Fig. 6. The fits using the model in Fig. 5 are shown also at lower frequencies but for demonstration purposes only. The actual fitting procedure itself was restricted to intermediate and high frequencies where the GB and bulk relaxations would be dominant (see also Fig. 5).

The impedance was additionally converted into the real parts of dielectric permittivity ε' in order to obtain further confirmation of the electrode blocking effect and the ionic charge transport (Fig. 7): the ε' vs. f spectra for the $Ce_{0.8}Gd_{0.1}Sm_{0.1}O_{1.9}$ sample show 3 distinct regimes, where the bulk and GB contributions are manifested by approximately frequency independent ε' plateaus each (as indicated in the graph), whereas the electrode interface contribution shows a uniform and linear increase of ε' with decreasing f. The bulk and GB plateaus are consistent with standard dielectric theory, whereas the interface again shows the typical signs for an electrode blocking effect.

The trends of $-Z''$ vs. Z', $-Z''$ vs. f and ε' vs. f shown in Figs. 5–7 were equivalent for the $Ce_{0.85}Gd_{0.15}O_{1.925}$, $Ce_{0.85}Sm_{0.15}O_{1.925}$ and $Ce_{0.8}Gd_{0.1}Sm_{0.1}O_{1.9}$ samples and ionic conductivity was indicated consistently.

3.3.2. *Resistivity vs. temperature trends*

The GB and bulk resistivity values ρ obtained from data fitting were plotted on a logarithmic scale vs. reciprocal temperature $1/T$ in Figs. 8 and 9, including the activation energies (E_A) determined from the slopes of the corresponding Arrhenius plots of $\ln(\rho)$ vs. $1/T$. Fig. 8 shows that all GB activation energies were in the range of 1 eV, typical for ionic charge transport. The GB resistivity values were considerably higher than all bulk values and confirm the notion that GBs constitute barriers for the ionic charge transport. The lowest GB resistivity was found for the $Ce_{0.85}Sm_{0.15}O_{1.925}$ sample, which may, therefore, be regarded preferential for IT-SOFC applications. Such preferential GB resistivity cannot be associated with the relatively small variations in grain size (see Fig. 3) and may well be an inherent property of the cationic dopant. In fact, the average grain size in the Sm doped sample is the lowest, emphasizing further the low GB resistivity. Such findings are confirmed by the bulk resistivity, showing optimum ionic conductivity for the Sm doped sample (Fig. 9). The ionic charge transport is known to be determined by the defect association energy and the local defect structure [50,51], which appear to be optimal in Sm doped ceria.

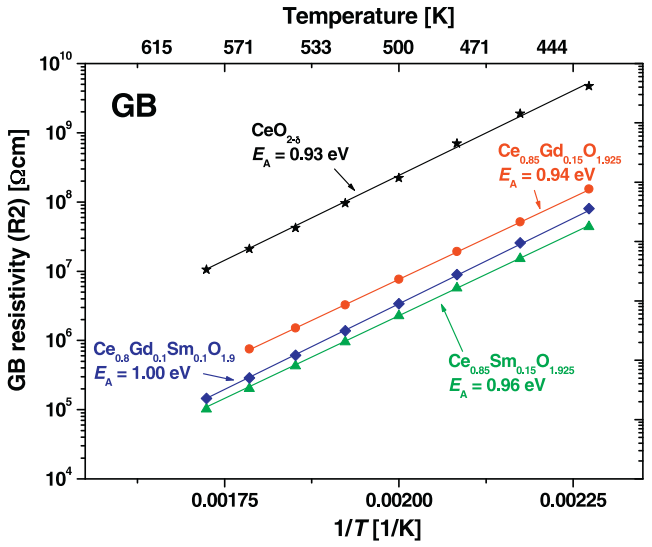

Fig. 8. Fitted GB resistivity (ρ) values obtained from the resistor R2 in the equivalent circuit (Fig. 5) plotted vs. reciprocal temperature $1/T$. The GB activation energies (E_A) are given in electron volts (eV) obtained from the respective $\ln(\rho)$ vs. $1/T$ plots.

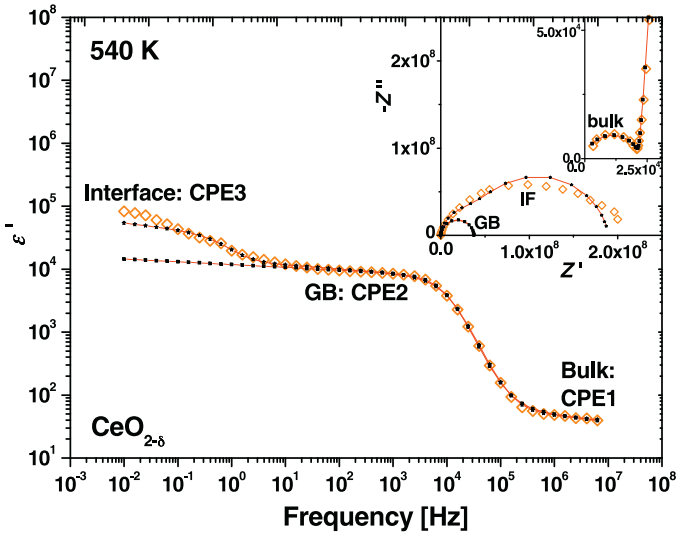

Fig. 10. Relative dielectric permittivity ε' vs. f for $CeO_{2-\delta}$. Open symbols (◊) represent measured data, squares (■) and solid lines represent equivalent circuit fits using the model presented in Fig. 5, (*) represent fits to the model in Fig. 11. *Figure insets*: complex impedance plots of $-Z''$ vs. Z' on different resistivity scales exhibiting interface (low f), GB (intermediate f) and bulk (high f) semicircles.

The GB activation energy for the preferential $Ce_{0.85}Sm_{0.15}O_{1.925}$ sample was 0.96 eV in excellent agreement with previous work on samples of the identical composition synthesized by the sol–gel method (0.97 eV) [52]. The overall GB resistivity at 500 K is decreased though in the work presented here by a factor of ≈100 as compared to such sol–gel samples [50] and by a factor of ≈400 as compared to recent $Ce_{0.8}Sm_{0.2}O_{2-\delta}$ sol–gel samples [26]. Hydrothermal synthesis appears to be a very effective way of synthesizing highly ionically conducting ceria ceramics. Recently, Moure et al. have claimed though that the GB resistivity encountered here can be further decreased by another factor of 8 using mechanosynthesis of ceria powders. Such samples had composition of $Ce_{0.8}Sm_{0.2}O_{1.9}$ [53]. The origin of this factor 8 may partially be debited to the higher ac amplitude of the impedance measurement signal of 500 mV used by Moure and coworkers, as compared to the 100 mV amplitude applied here. The GB resistivity in ionic conductors is commonly influenced by the ac amplitude, because GBs act as Schottky barriers resulting in a non-ohmic (non-linear) GB resistance [10]. In fact, the intrinsic bulk ionic resistivity in the work by Moure et al. [53] was lower than in the sample presented here by a factor of only 2, which is a realistic decrease as a result of the higher Sm doping level. Bulk ionic charge transport is usually ohmic (linear) [10] and, therefore, the ac test signal amplitude is irrelevant and the bulk resistivity values can be compared unambiguously.

The bulk E_A values here were all in the range of 0.85 eV as shown in Fig. 9, except for the $CeO_{2-\delta}$ curve where both the bulk ρ and E_A values are rather low for ionic charge transport.

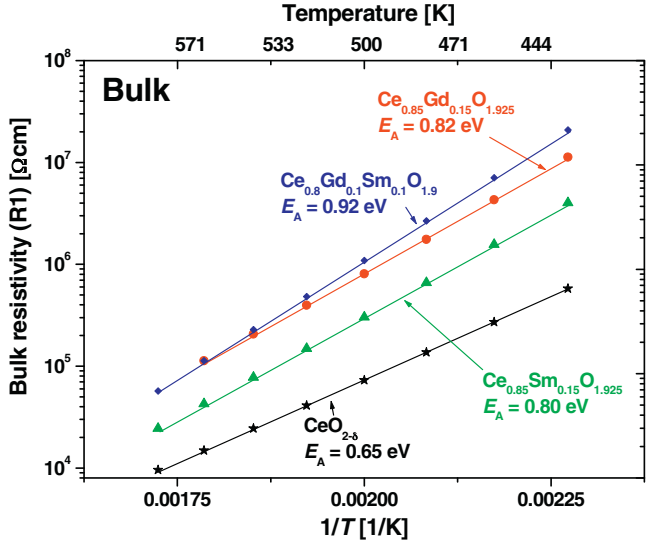

Fig. 9. Fitted bulk resistivity values obtained from the resistor R1 in the equivalent circuit (Fig. 5) plotted vs. $1/T$. The bulk activation energies (E_A) are given in eV.

3.3.3. *Undoped $CeO_{2-\delta}$*

This points toward a significant electronic contribution, which is supported by the fact that the ε' vs. f curve for $CeO_{2-\delta}$ (Fig. 10) did not show the typical behavior of ionic conductors at low f mentioned above (Fig. 7). Fig. 10 shows that the interface dielectric permittivity approaches another ε' plateau at the low frequency end, consistent with the behaviour of a conventional dielectric relaxation as described by an RC element. The first Figure Inset demonstrates that the GB semicircle in $-Z''$ vs. Z' plots is overlaid by a conventional interface (IF) semicircle. Such semicircle overlap occurs, because the IF and GB time constants τ are similar. In the ε' vs. f notation the IF and GB relaxations are clearly separated though, and two equivalent circuit fits were performed: one with a circuit containing a series of 2 R-CPE elements for the bulk and GB relaxations at high/intermediate f (■), and another fit with 3 series R-CPE elements for the bulk, GB and interface (IF) relaxations over the full frequency range (*). Without an interface "pike" structure in the $-Z''$ vs. Z' plot and the interface response being consistent with a conventional RC element, the signs of a blocking electrode are missing in $CeO_{2-\delta}$. Ionic charge transport is not indicated and an electronic contribution appears to be dominant.

The second Fig. 10 inset shows the same data as in the first Inset but is magnified at the high frequency end. The $CeO_{2-\delta}$ bulk semicircle can be seen clearly, whereas the GB semicircle appears to be much larger in size, which indicates a large difference between bulk and GB resistivity. This confirms the findings of Figs. 8 and 9 and is illustrated in plots of $-Z''$ vs. f depicted in Fig. 11: two peaks can be seen, which are largely separated in magnitude on both the

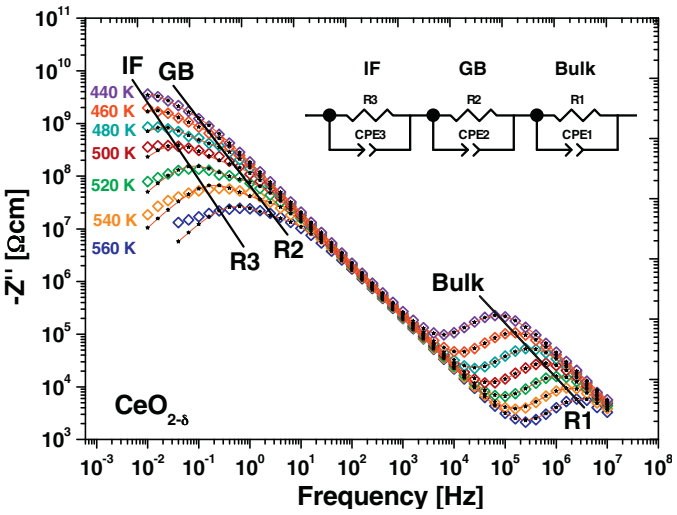

Fig. 11. Imaginary part of the impedance ($-Z''$) plotted vs. frequency for $CeO_{2-\delta}$. Two relaxation peaks are displayed, one double peak structure for the GB and the interface (IF) and one for the bulk dielectric relaxation. Open symbols (◊) represent measured data, stars (*) and solid lines represent equivalent circuit fits using the model presented in the figure.

$-Z''$ *y*-axis and the frequency *x*-axis. It has to be noted though that the high resistivity peak at low frequency is in fact a double peak, consisting of the GB and IF contributions (as indicated). The low $CeO_{2-\delta}$ bulk resistivity is believed to be a result of incomplete oxygenation and the formation of oxygen vacancies (δ). Such vacancies would be compensated by partial reduction of Ce^{4+} to Ce^{3+}, leading to electronic hopping conductivity [54]. Fully oxygenated CeO_2 is expected to be insulating, and the formation of oxygen vacancies may be the only plausible mechanism to induce perceptible conductivity into undoped ceria oxide. The high GB resistivity in $CeO_{2-\delta}$ (Figs. 8 and 11) suggests that the GB areas showed significantly higher levels of oxygenation as the bulk, which is a common feature in electroceramic materials. Generally, the MW synthesized $CeO_{2-\delta}$ sample seems little suitable for ionic conductor applications in contrast to the rare-earth doped specimen. The equivalent circuit for $CeO_{2-\delta}$ with a series of 3 R-CPEs is shown in Fig. 11, giving an imperfect match between data and model at low frequencies due to the strong overlap of GB and IF relaxations (Figs. 10 and 11).

4. Conclusions

Phase pure rare-earth Sm and Gd doped and undoped ceria oxide ceramics with large surface area were produced successfully using microwave-assisted hydrothermal synthesis leading to high sintering activity of the nano-powders. Impedance spectroscopy measurements on sintered ceramics confirmed ionic charge transport in rare-earth doped ceria, whereas the undoped $CeO_{2-\delta}$ parent compound exhibited signs of electronic conduction, most likely due to mixed valent Ce^{3+}/Ce^{4+} electron hopping. Deconvolution of GB and intrinsic bulk ionic conductivity revealed that GBs constitute barriers for ionic charge transport, with the Sm doped ceria $Ce_{0.85}Sm_{0.15}O_{1.925}$ exhibiting the highest GB ionic conductivity. The highest intrinsic bulk ionic conductivity was detected for the $Ce_{0.85}Sm_{0.15}O_{2-\delta}$ ceramic as well, which may, therefore, be favorable for IT-SOFC applications.

Acknowledgements

J.P.-G. acknowledges financial help from the Community of Madrid (Materyener S2009/PPQ-1626) and a PhD scholarship from the Universidad Complutense de Madrid. R.S. acknowledges the Ministerio de Ciencia e Innovacion (MICINN) for granting a Ramon y Cajal Fellowship. Furthermore, this work was supported by the MICINN through grants no. MAT 2007-31034 and MAT 2010-19837-CO6-03. The authors wish to express their gratitude to Dra. Maria-José Torralvo for technical assistance with the BET measurements, to Prof. Jacobo Santamaria and Prof. Carlos León for allowing use of and for assistance with the impedance spectroscopy facilities, and to Prof. Alberto Rivera-Calzada for useful discussions.

References

[1] C. Keegan, J. Wincewicz, S. Cooper, J. Power Sources 140 (2005) 280.
[2] D. Chen, R. Ran, K. Zhang, J. Wang, Z. Shao, J. Power Sources 188 (2009) 96.
[3] M. Dokiya, Solid State Ionics 152–153 (2002) 383.
[4] D.J.L. Brett, A. Atkinson, N.P. Brandon, S.J. Skinner, Chem. Soc. Rev. 37 (2008) 1568.
[5] J. Garcia-Barriocanal, A. Rivera-Calzada, M. Varela, Z. Sefroui, E. Iborra, C. Leon, S.J. Pennycook, J. Santamaria, Science 321 (2008) 676.
[6] N.Q. Minh, J. Am. Ceram. Soc. 76 (1993) 563.
[7] C. León, M.L. Lucía, J. Santamaria, Phys. Rev. B 55 (1997) 882.
[8] B.C.H. Steele, Solid State Ionics 134 (2000) 3.
[9] S. Zha, C. Xia, G. Meng, J. Power Sources 115 (2003) 44.
[10] X. Guo, R. Waser, Prog. Mater. Sci. 51 (2006) 151.
[11] H.L. Tuller, Solid State Ionics 131 (2000) 143.
[12] A. Trovarelli, Catal. Rev. Sci. Eng. 38 (1996) 439.
[13] E. Matijevic, W.P. Hsu, J. Colloid Interface Sci. 118 (1987) 506.
[14] T.J. Kirk, J. Winnick, J. Electrochem. Soc. 140 (1993) 3494.
[15] F. Bondioli, A. Bonamartini Corradi, T. Manfredini, C. Leonelli, R. Bertoncello, Chem. Mater. 12 (2000) 324.
[16] F. Bondioli, P. Veronesi, C. Leonelli, T. Manfredini, in: G. Muller (Ed.), Ceramics—Processing, Reliability, Tribology and Wear, vol. 12, Wiley-VCH, Weinheim, 1999, pp. 11–16.
[17] N.C. Wu, E.W. Shi, Y.Q. Zheng, W.J. Li, J. Am. Ceram. Soc. 85 (2002) 2462.
[18] J. Prado-Gonjal, A.M. Arévalo-López, E. Morán, Mater. Res. Bull. 46 (2011) 222.
[19] J. Prado-Gonjal, R. Schmidt, D. Ávila, U. Amador, E. Morán, J. Eur. Ceram. Soc. 32 (2012) 611.
[20] J.-H. Lee, N. Kumagai, T. Watanabe, M. Yoshimura, Solid State Ionics 151 (2002) 41.
[21] S. Komarneni, Curr. Sci. 85 (2003) 1730.
[22] J. Prado-Gonjal, D. Avila, M.E. Villafuerte-Castrejón, F. González García, L. Fuentes, R.W. Gómez, J.L. Pérez-Mazariego, V. Marquina, E. Morán, Solid State Sci. 13 (2011) 2030.
[23] C.S. Riccardi, R.C. Lima, M.L. dos Santos, P.R. Bueno, J.A. Varela, E. Longo, Solid State Ionics 180 (2009) 288.
[24] F. Bondioli, A.M. Ferrari, L. Lusvarghi, T. Manfredini, S. Nannarone, L. Pasquali, G. Selvaggi, J. Mater. Chem. 15 (2005) 1061.
[25] G.B. Balazs, R.S. Glass, Solid State Ionics 76 (1995) 155.
[26] S. Ramesh, V. Prashanth Kumar, P. Kistaiah, C. Vishnuvardhan Reddy, Solid State Ionics 181 (2010) 86.
[27] A. Bonamartini Corradi, F. Bondioli, A.M. Ferrari, T. Manfredini, Mater. Res. Bull. 41 (2006) 38.
[28] G.A. Tompsett, W.C. Conner, K.S. Yngvesson, ChemPhysChem 7 (2006) 296.
[29] J. Rodriguez-Carvajal, J. Phys. B 192 (1993) 55.
[30] S. Brunauer, P.H. Emmett, E. Teller, J. Am. Chem. Soc. 60 (1938) 309.
[31] B.H. Davis, J. Phys. Chem. 90 (1986) 4702.
[32] Y.S. Bae, R.Q. Snurr, O. Yazaydin, Langmuir 26 (2010) 5475.
[33] R. Schmidt, in: P.B. Lin (Ed.), Ceramic Materials Research Trends, Novascience Publishers, Hauppauge, 2007, p. 321.
[34] P. Scherrer, Göttinger Nachrichten Gesell. 2 (1918) 98.
[35] H.J. Whitfield, D. Roman, A.R. Palmer, J. Inorg. Nucl. Chem. 28 (1966) 2817.
[36] G. Brauer, H. Gradinger, Z. Anorg, Allgem. Chem. 276 (1954) 209.
[37] T.S. Zhang, L.B. Kong, Z.Q. Zeng, H.T. Huang, P. Hing, Z.T. Xia, J. Kilner, J. Solid State Electrochem. 7 (2003) 348.
[38] C.G. Schull, J. Am. Chem. Soc. 70 (1948) 1405.
[39] F. Rouquerol, J. Rouquerol, K. Sing, Adsorption by Powders and Porous Solids, Academic Press, France, 1999.
[40] R.J. Brook, Concise Encyclopedia of Advanced Ceramic Materials, Pergamon Press, Oxford, UK, 1991, p. 275.
[41] C. Pan, D. Zhang, L. Shi, J. Solid State Chem. 181 (2008) 1298.
[42] S. Pavasupree, Y. Suzuki, S. Pivsa-Art, S. Yoshikawa, Ceram. Int. 31 (2005) 959.
[43] Y. He, Powder Technol. 155 (2005) 1.
[44] J.T.S. Irvine, D.C. Sinclair, A.R. West, Adv. Mater. 2 (1990) 132.
[45] E. Barsukov, J.R. Macdonald, Impedance Spectroscopy: Theory, Experiment and Applications, John Wiley & Sons Inc., Hoboken, USA, 2005.
[46] A. Díez, R. Schmidt, A.E. Sagua, M.A. Frechero, E. Matesanz, C. Leon, E. Morán, J. Eur. Ceram. Soc. 30 (2010) 2617.
[47] K. Funke, R. Hoppe, Solid State Ionics 40–41 (1990) 200.

[48] R. Schmidt, W. Eerenstein, T. Winiecki, F.D. Morrison, P.A. Midgley, Phys. Rev. B 75 (2007) 245111.
[49] A. Rivera-Calzada, M.R. Diaz-Guillen, O.J. Dura, G. Sanchez-Santolino, T.J. Pennycook, R. Schmidt, F.Y. Bruno, J. Garcia-Barriocanal, Z. Sefrioui, N.M. Nemes, M. Garcia-Hernandez, M. Varela, C. Leon, S.T. Pantelides, S.J. Pennycook, J. Santamaria, Adv. Mater. 23 (2011) 5268.
[50] J.A. Kilner, Solid State Ionics 129 (2000) 13.
[51] H. Yoshida, T. Inagaki, K. Miura, M. Inaba, Z. Ogumi, Solid State Ionics 160 (2003) 109.
[52] C. Sánchez-Bautista, A.J. dos Santos-García, J. Peña-Martínez, J. Canales-Vázquez, Bol. Soc. Esp. Ceram. V 49 (2010) 7.
[53] A. Moure, C. Moure, J. Tartaj, J. Power Sources 196 (2011) 10543.
[54] H.L. Tuller, A.S. Nowick, J. Phys. Chem. Solids 38 (1977) 859.